

LARGE EDDY SIMULATIONS OF TURBULENT COUETTE-POISEUILLE AND COUETTE FLOWS INSIDE A SQUARE DUCT

Hsin-Wei Hsu, Jian-Bin Hsu, Wei Lo and Chao-An Lin*

Department of Power Mechanical Engineering
National Tsing Hua University, Hsinchu 30013, TAIWAN

ABSTRACT

Turbulent Couette-Poiseuille and Couette flows at different mean strain rates, (velocity ratio of Couette wall to bulk flow, $r = 0.6 \sim 3.15$), in a square duct at a bulk Reynolds number $\approx 10,000$ are investigated by large eddy simulation. Simulations are conducted with $160 \times 160 \times 256$ grids. Secondary flow near the Couette wall shows a gradual change of vortex size and position as the moving wall velocity increased, where the two clockwise rotating vortices gradually merge in tandem with speed of the moving wall and form a large clockwise vortex. A linear relation is observed to exist between the angle of the two vortices and the parameter r , and the angle saturates beyond $r \sim 2.06$. Also, at $0.6 < r < 1.6$, together with a small counter-clockwise corner vortex, this vortex pattern is similar to that observed in the corner region of the duct flow with a free surface. Near the moving wall due to the reduction of the streamwise velocity fluctuation at the moving wall, turbulence structure gradually moves towards a rod-like axi-symmetric turbulence, and as r increases beyond 1.2, turbulence reverts to the disk-like structure.

Introduction

Turbulent flows inside a square duct are of considerable engineering interest, such as in heat exchangers or internal cooling passages of turbine blade (Iacovides & Launder (1995)). The most studied flow is the turbulent Poiseuille type inside a square duct (Madabhushi & Vanka (1991), Gavrilakis (1992), and Huser & Biringen (1993)), which is characterized by the existence of secondary flow of Prandtl's second kind and is not observed in circular ducts nor in laminar rectangular ducts. The secondary flow is a mean circulatory motion perpendicular to the streamwise direction driven by the anisotropy of turbulence.

Although weak in magnitude (only a few percent of the streamwise bulk velocity), the effects of secondary flow on the momentum and heat transfer are noticeable (Huser & Biringen (1993); Iacovides & Launder (1995)). Thus, factors affecting the secondary flow patterns within turbulent duct flows were actively pursued, such as, bounding wall geometry, non-isothermal effect, free surface, system rotation, and Reynolds number (Vazquez & Metais (2002), Pallares & Davidson (2002), Brogolia *et al.* (2003), Uhlmann *et al.* (2007)). The above investigations have implied that with careful manipulation, the secondary flow can enhance

momentum transport or heat transfer in different industrial devices.

However, few studies focused on the effect of the moving wall on the flow and hence secondary flow structure. Previous studies on turbulent Couette-Poiseuille flows have been conducted on simple plane channels and different turbulence statistics and structures between the stationary and moving wall were identified (Thurlow & Klewicki (2000), Kuroda *et al.* (1993), Hwang & Lin (2003)). For Couette-Poiseuille duct flow, Lo & Lin (2006) found that the secondary flow structure correlates with the ratio of the speed of the moving wall and duct bulk flow, albeit the ratio was less than 1.17.

Thus the present study aims to investigate how the flow structure within the square duct changes in response to the increase of the Couette wall velocity. At a fixed bulk Reynolds number, the flow would migrate from the Couette-Poiseuille duct flow to a Couette duct flow. Large eddy simulation is used to compute turbulent Couette-Poiseuille and Couette flows at different mean strain rates, (velocity ratio of Couette wall to bulk flow, $r = 0.6 \sim 3.15$), in a square duct at a bulk Reynolds number $\approx 10,000$. Issues to be addressed are: the correlation of the secondary flow and hence its vorticity transport mechanism to the Couette strain rate, and the change of the turbulence structures.

Governing Equations and Turbulence Modeling

The governing equations for the LES simulation are obtained by applying the filtering operation. The grid-filtered, incompressible Navier-Stokes equations assume the following forms:

$$\frac{\partial \rho \bar{u}_i}{\partial t} + \frac{\partial (\rho \bar{u}_i \bar{u}_j)}{\partial x_j} = -\frac{\partial \bar{P}}{\partial x_i} + \frac{\partial}{\partial x_j} \left[\mu \left(\frac{\partial \bar{u}_i}{\partial x_j} + \frac{\partial \bar{u}_j}{\partial x_i} \right) \right] - \frac{\partial \tau_{ij}^s}{\partial x_j} \quad (1)$$

where, $\tau_{ij}^s = \rho (\overline{u_i u_j} - \bar{u}_i \bar{u}_j)$ is the sub-grid stress due to the effects of velocities being not resolved by the computational grids and has to be modeled. Here, $U_i = \langle \bar{u}_i \rangle$ and the Reynolds stress is $\langle u_i' u_j' \rangle$. In the present study, the dynamic model (Germano *et al.* (1991)) is adopted to model the sub-grid stress (SGS),

$$\tau^a = \tau_{ij}^s - \frac{\delta_{ij}}{3} \tau_{kk}^s = -2C_D \bar{\Delta}^2 |\bar{S}| \bar{S}_{ij} \quad (2)$$

*Corresponding author, calin@pme.nthu.edu.tw

August 28 - 30, 2013 Poitiers, France

where δ_{ij} is the Kronecker delta, $S_{ij} = \frac{\partial \bar{u}_i}{\partial x_j} + \frac{\partial \bar{u}_j}{\partial x_i}$, and, Δ defined as $(\Delta x \Delta y \Delta z)^{1/3}$ is the filter width, where the mesh size is a parameter of the filtering operator. For dynamic model, the model coefficient C_D is allowed to be a function of space and time. Following Lilly (1992), the coefficient is obtained using the least square approach.

Numerical Algorithms and Boundary Conditions

A semi-implicit, fractional step method and the finite volume method are employed to solve the filtered incompressible Navier-Stokes equations (Hsu *et al.* (2011, 2012)). Spatial derivatives are approximated using second-order central difference schemes. The non-linear terms are advanced with the Adams-Bashforth scheme in time, whereas the Crank-Nicholson scheme is adopted for the diffusion terms. The discretized algebraic equations from momentum equations are solved by the preconditioned Conjugate Gradient solver. In each time step a Poisson equation is solved to obtain a divergence free velocity field. Because the grid spacing is uniform in the streamwise direction, together with the adoption of the periodic boundary conditions, Fourier transform can be used to reduce the 3-D Poisson equation to uncoupled 2-D algebraic equations. The algebraic equations are solved by the direct solver using LU decomposition.

Flows considered here are fully developed, incompressible turbulent Couette-Poiseuille and Couette flows inside a square duct. The computational domain consists of $D \times D \times 2\pi D$ (D is the width of the duct) in the horizontal (x), vertical (y) and streamwise (z) directions, respectively. Here, u , v and w are used to denote, respectively, the velocity components in the horizontal, vertical, and streamwise directions. The adopted length of the streamwise computational domain ($2\pi D$) is based on the earlier DNS and LES studies of Huser & Biringen (1993) and Madabhushi & Vanka (1991) and two-point streamwise velocity correlations were used to check its adequacy to capture the longest structure.

No-slip boundary conditions for the velocity components are applied at the four bounding walls and periodic boundary condition is employed in the streamwise direction at the inlet and outlet of the square duct. Top wall ($y=D$) is either stationary or moving in the positive streamwise direction, while other bounding walls are at rest. Grid ($160 \times 160 \times 256$) is symmetrically clustered using hyperbolic tangent functions towards the walls on the cross-plane of the duct with $\Delta x^+, \Delta y^+ \sim 0.25 - 16.77$. In the streamwise direction, the grid is uniformly distributed with $\Delta z^+ \sim 30.3$. The present results show marginal difference with complementary LES ($192 \times 192 \times 192$) and DNS ($192 \times 192 \times 384$) studies on turbulence quantities for duct Poiseuille and Couette flows. Also, the present SGS contribution to momentum transport was estimated to be less than 3% of its resolved stress counterpart. After the flow reached the statistically stationary state, the simulation was carried out for another 30 eddy turnover time (D/u_τ) to assemble the mean flow field and turbulence statistics, which are consistent with the 60 eddy turnover time data. Validations of the predicted results with DNS data are referred to Fig. 5.

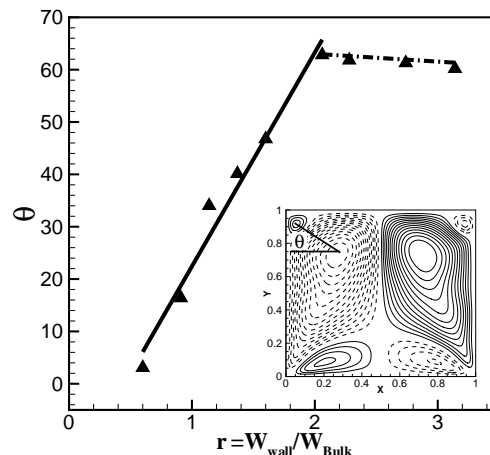


Figure 3. Angles between twin vortex cores against the parameter r near the top corners. Solid line: least square line for $r < 2.06$; Dash-dot line: least square line for $r > 2.06$; \blacktriangle : θ_1 .

Results

Flows considered are fully developed, incompressible turbulent Couette-Poiseuille flows inside a square duct where the basic flow parameters are summarized in Table 1, where case P is the pure Poiseuille flow, cases CP's are Couette-Poiseuille flows at different ratios of wall velocity and pressure gradient and C is pure Couette flow. Also included in this table is the turbulent plane Couette-Poiseuille flow conducted by Kuroda *et al.* (1993) for comparison purposes. Reynolds number based on the bulk velocity (Re_{bulk}) is kept around 10,000 for all cases simulated and the importance of Couette strain rate in this combined flow field can be indicated by the ratio $r = (W_w / W_{Bulk})$. To maintain the constant bulk Reynolds number, the driving pressure gradient is modified at each time step by the bulk Reynolds number.

Mean and turbulence fields

Mean streamwise velocity distributions from the top wall along the wall bisector, i.e. $x/D=0.5$, at different mean Couette strain rates are shown in Figure 1 compared with DNS data of Moser *et al.* (1999) and Iwamoto *et al.* (2002). For cases P-CP1 and CP6-C, the velocity distributions follow closely the 2D channel flow DNS data. However, at medium Couette velocity, i.e. (CP2-CP5, i.e. $r=0.91 \sim 1.6$), due to the reduction of shear rate, departures from the logarithmic distributions are observed. It should be noted that for all cases considered logarithmic distributions prevail at the bottom wall, except in the vicinity of the side wall. The influence of the moving wall also can be observed from the instantaneous flow structure in Fig. 1 (b), showing cross sectional view of the longitudinal velocity fluctuations. It is clear that as the increase of moving wall, the turbulence structures are gradually suppressed by low mean shear rate. This damping is most significant as the Couette velocity is near the bulk velocity, i.e. CP3 case. However, beyond $r > 2.06$, the streaky structure is similar to its Poiseuille duct flow counterpart.

Streamlines of mean secondary flow for cases P to C are shown in Figure 2. Due to the symmetrical nature of the flow, only half the domain is shown here for simplicity. The

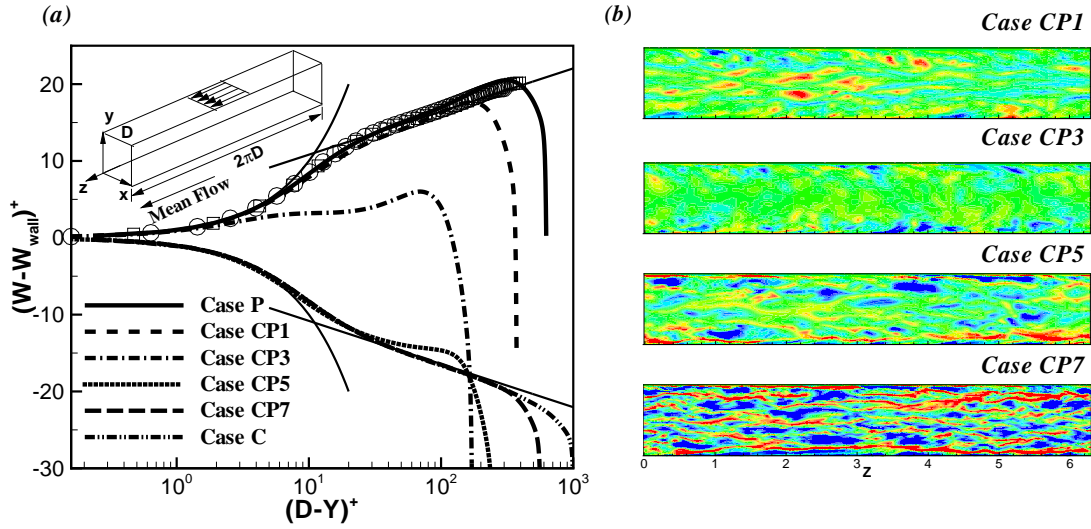


Figure 1. (a) Geometry and mean streamwise velocity along the wall-bisector. \square : Moser *et al.* (1999); \circ : Iwamoto *et al.* (2002). (b) Cross-sectional view of longitudinal velocity fluctuation ($Y/D=0.98$) at different Couette strain rates $r=0.6$ (CP1), 1.14 (CP3), 1.6 (CP5), 2.28 (CP7).

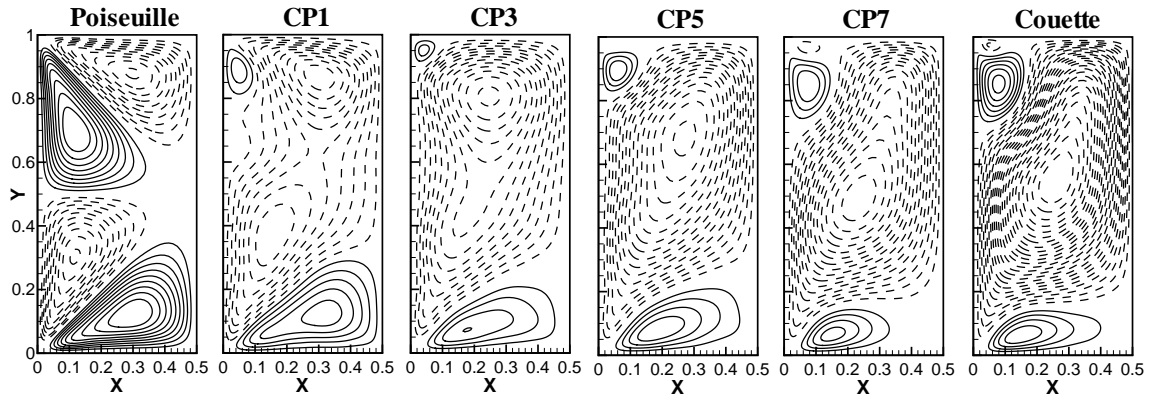


Figure 2. Streamlines of mean secondary flow for cases P to C.

Table 1. The flow conditions for simulated cases; W_w denotes the velocity of the moving wall and W_{Bulk} is the bulk velocity; $Re_\tau = u_\tau D / \nu$ (t =top moving wall, b =bottom stationary wall); $Re_c = \frac{W_w D}{\nu}$; $r = \frac{W_w}{W_{Bulk}}$.

	Case P	Case CP1	Case CP2	Case CP3	Case CP4	Case CP5	Case CP6	Case CP7	Case CP8	Case C	Kuroda et al. (1993)
Re_τ	616	412	333	327	402	498	681	775	970	1225	35
$Re_{\tau b}$	616	593	583	579	572	567	551	541	522	553	308
Re_{Bulk}	10000	10000	10000	10000	10000	10000	10000	10000	10000	10890	5178
Re_c	0	6000	9136	11420	13704	15988	20556	22840	27408	34260	6000
r	0	0.6	0.91	1.14	1.37	1.60	2.06	2.28	2.74	3.15	1.16

vortex structure is clearly visible, where solid and dashed lines represents counter-clockwise and clockwise rotation, respectively. The presence of the moving wall does influence the patterns of the secondary flow, where the two clockwise rotating vortices gradually merge in tandem with speed of the moving wall near the Couette wall. Near the

moving wall, the distribution of these secondary structure consisting of a small and a large vortex is similar to that of free surface problem observed by Grega *et al.* (1995); Brogolia *et al.* (2003). However, as the wall velocity further increases for $r > 1.6$, the fast moving wall is responsible for the formation of another smaller clockwise rotating vor-

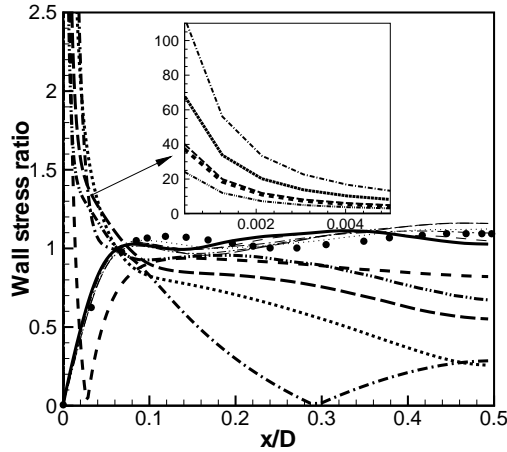


Figure 4. Wall stress variation from moving (thick line) and stationary wall (thin line)-cases P to C. Line legend as for Fig. 1; •: Huser & Biringen (1993).

text near the top corner. On the other hand, along the bottom corner bisector the secondary flow is still pointing towards the corner the same as in turbulent Poiseuille flow. The angle formed by the horizontal x axis and the line joining the two vortex cores is calculated and plotted against the parameter r defined by W_w/W_{bulk} which can be interpreted as the non-dimensional moving wall velocity. A linear relation exists between the angle and the parameter r , as shown in Figure 3. For $r > 2.06$, the angle saturates and remains at around 62° .

Local wall stress distributions along the top moving and bottom stationary walls are shown in Fig. 4. For all the cases considered in Table 1, the distributions at the stationary wall follow that the turbulent Poiseuille flow and have good agreement with DNS data of Huser & Biringen (1993). On the other hand, wall stresses along the moving wall show dramatic different profiles, especially near the top corner. As the mixed wall corner is approached, due to the high velocity gradient between the fast moving wall and the nearby slow moving fluid, wall-shear stress of case CP3 ($r = 1.14$) reaches a large but finite value with the maximum value around 110. Also, away from the top corner, shear stress first decreases in response to reduction of strain due to the increase of the wall velocity for $r < 1.4$. The zero wall stress location, which roughly coincides with the zero $\partial W/\partial y$ region, moves towards the central region as the wall velocity increases. As the moving wall velocity increases further, the wall stress increases and distributions approach their bottom wall counterparts.

Detailed examinations of the turbulence quantities normalized by the stationary wall shear stress can be seen in Fig. 5, showing the predicted turbulence production, and intensities along the wall bisector at $x/D=0.5$. Here, the DNS data of Poiseuille flow (Huser & Biringen (1993)), plane channel flow ($Re_\tau = 395$, Moser *et al.* (1999), $Re_\tau = 300$, Iwamoto *et al.* (2002)), and plane Couette-Poiseuille flow ($Re_\tau = 300$, Kuroda *et al.* (1993)) are also included for comparisons. The r value of the plane Couette-Poiseuille flow is close to 1.14 of CP3 case. In Figs. 5 (a)-(d), the turbulence production and turbulence intensities distributions from the duct center towards the bottom wall are similar to those found in Poiseuille duct flow (Huser & Biringen (1993))

and plane channel flow Moser *et al.* (1999) and Iwamoto *et al.* (2002). Good agreements with DNS data show the quality of the present predictions. Near the moving wall, the turbulence level is decreased first in tandem with the increase of moving wall velocity. However, beyond $r > 1.2$, due to the high velocity gradient between the fast moving wall and nearby slow moving fluid, turbulence production and turbulence intensity gradually increase. This change of turbulence is in response to the variation of local strain and hence stress. Also, as shown in Fig. 5(b), the ratio of the maximum intensity of the moving and stationary walls of the Couette duct flow is similar to the ratio of the respective wall shear stresses, which is around 2.3.

Turbulence structure

The invariants of the Reynolds stress tensors are defined as $II = -(1/2)b_{ij}b_{ij}$, $III = (1/3)b_{ij}b_{jk}b_{ki}$, where $b_{ij} = \langle u'_i u'_j \rangle / \langle u'_k u'_k \rangle - 1/3\delta_{ij}$. A cross-plot of $-II$ versus III forms the anisotropy invariant map (AIM). All realizable Reynolds stress invariants must lie within the Lumley triangle (Lumley (1978)). The region is bounded by three lines, namely two component state, $-II = 3(III + 1/27)$, and two axi-symmetric states, $III = \pm(-II/3)^{3/2}$.

AIM of Couette Poiseuille and Couette flows at several horizontal locations are presented in Figure 6. Here DNS data of channel flow (Iwamoto *et al.* (2002)) and plane Couette-Poiseuille flow (Kuroda *et al.* (1993)) are also included for comparison. Near the stationary wall ($y/D \leq 0.5$), turbulence behavior of different Couette-Poiseuille flows resemble those of the plane Poiseuille flow. In particular, the turbulence structure is similar to the plane channel flow, where turbulence approaches two component state near the stationary wall due to highly suppressed wall-normal velocity fluctuation. It moves toward the one-component state till $y^+ \sim 8$ (Antonia *et al.* (1977), Vazquez & Metais (2002)) because of the dramatic increase of streamwise fluctuation in the near wall region and then follows the positive III axi-symmetric branch (disk-like turbulence, Lee & Reynolds (1985)) towards the isotropic state at the duct center. Near the moving wall, on the other hand, due to the reduction of the streamwise velocity fluctuation at the moving wall, turbulence structure of cases CP1 to CP4 become a rod-like axi-symmetric turbulence (negative III) at $x/D=0.5$. AIM path from plane Couette-Poiseuille by Kuroda *et al.* (1993) also shows this behavior, though it is at a lower Reynolds number. The AIM path at $x/D=0.5$ also reveals that the anisotropy level (magnitude of II) near the moving wall is lower than near the stationary wall. Away from the middle plane $x/D=0.5$, turbulence structures gradually restore to boundary layer like profiles and the difference between AIM path of stationary and moving boundary layer is lessened. As the wall velocity increases further for $r > 1.2$, the rod like structure disappears, and turbulence reverts to the disk like structure, as is shown in Fig 6. At other axial locations, the AIM patterns at the stationary wall are similar to that at $x/D = 0.5$, except at $x/D=0.015$, where the AIM follows the two-component branch toward one component limit. Also, for the Couette duct flow, AIM paths are similar to the duct Poiseuille flow.

Mean Streamwise Vorticity

The secondary flow structure is closely related to the mean vorticity $\Omega_z = \frac{\partial \langle v \rangle}{\partial x} - \frac{\partial \langle u \rangle}{\partial y}$. Thus, it will be beneficial to examine the vorticity transport equation (Brogolia

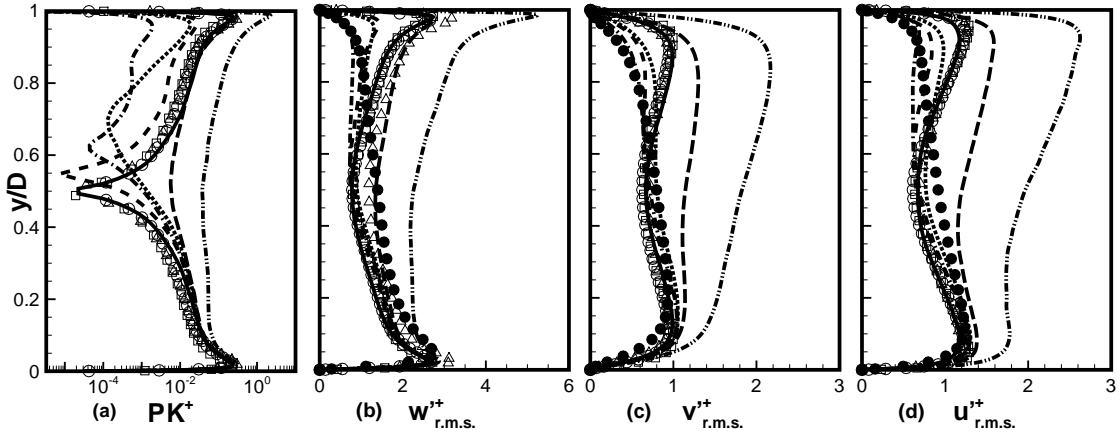


Figure 5. Turbulence production, kinetic energy and intensities along the wall bisector for cases P to C. Legend for lines see figure 1; \triangle symbol: Huser & Biringen (1993); \bullet symbol: Kuroda *et al.* (1993); \square symbol: Moser *et al.* (1999); \circ symbol: Iwamoto *et al.* (2002).

et al. (2003)), and is shown as follows.

$$\begin{aligned}
 \underbrace{U^+ \frac{\Omega_z^+}{\partial x^+} + V^+ \frac{\partial \Omega_z^+}{\partial y^+}}_{\text{Convection}} &= \underbrace{\frac{1}{Re_{Bulk}} \left(\frac{\partial^2 \Omega_z^+}{\partial x^{+2}} + \frac{\partial^2 \Omega_z^+}{\partial y^{+2}} \right)}_{\text{Viscous diffusion}} \\
 &+ \underbrace{\left(\frac{\partial^2}{\partial x^{+2}} - \frac{\partial^2}{\partial y^{+2}} \right) (-\langle u^+ v^+ \rangle)}_{\text{Shear stress production}} \\
 &+ \underbrace{\frac{\partial^2}{\partial x^+ \partial y^+} (\langle u'^{+2} \rangle - \langle v'^{+2} \rangle)}_{\text{normal stress production}} \\
 &+ \underbrace{\left(\frac{\partial^2}{\partial x^{+2}} - \frac{\partial^2}{\partial y^{+2}} \right) \langle \tau_{xy}^+ \rangle - \frac{\partial^2}{\partial x^+ \partial y^+} (\langle \tau_{xx}^+ \rangle - \langle \tau_{yy}^+ \rangle)}_{\text{unresolved SGS production}}
 \end{aligned} \quad (3)$$

which represents balances among convection, viscous diffusion and resolved and unresolved shear stress and anisotropy of normal stress productions. The unresolved SGS production of vorticity is marginal, which is less than 1% of the resolved ones.

Influences of the Couette velocity on the relative importance of transport terms in Eq. 3 can be referred to Fig. 7, where the filled and open symbols represent transport contributions at the maximum normal stress production along vertical cross sections across the centers of the counter-clockwise (inner) and clockwise (outer) vortices, respectively, at the top wall, as shown in Fig. 2.

For the inner corner vortex shown in Fig. 7, the generation of vorticity is dominated by the normal stress transport ($r \leq 1.6$) and viscous diffusion ($r \geq 1.6$). The shear stress production is observed to decay in tandem with the increase of the Couette velocity for ($r \leq 1.6$). This indicates

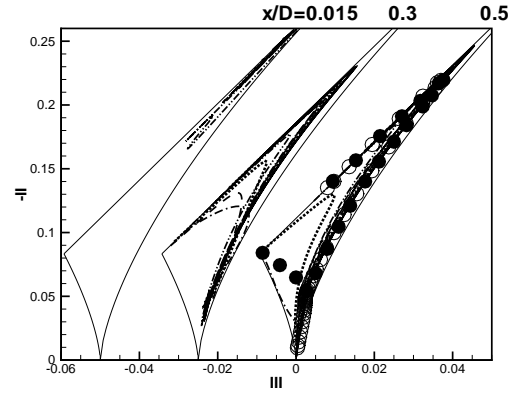


Figure 6. Anisotropy invariant map for cases P to C at different locations. Legend for lines see figure 1; \bullet : Kuroda *et al.* (1993); \circ : Iwamoto *et al.* (2002).

the gradual transition from the Poiseuille flow type (Madabhushi & Vanka (1991); Huser & Biringen (1993)) to the free surface flow type (Brogolia *et al.* (2003)). Beyond $r > 1.6$, shear stress contribution increases and exceeds that of the normal stress production, which is due to the emergence of another smaller vortex at the top corner. For the outer vortex, normal stress production is balanced by shear stress production and viscous diffusion, though the viscous diffusion becomes dominant at larger Couette velocity ($r > 2$).

Conclusions

Turbulent Couette-Poiseuille and Couette flows at different mean strain rates, (velocity ratio of Couette wall to bulk flow, $r = 0.6 \sim 3.15$), in a square duct at a bulk Reynolds number $\approx 10,000$ are investigated by large eddy simulation. Simulations are conducted with $160 \times 160 \times 256$ grids. The present SGS contribution to momentum transport was estimated to be less than 3% compared to its resolved stress counterpart and the unresolved SGS production of vorticity is less than 1% of the resolved ones.

Influences of the top moving wall on the flow and turbulence structure near the stationary bottom wall are not

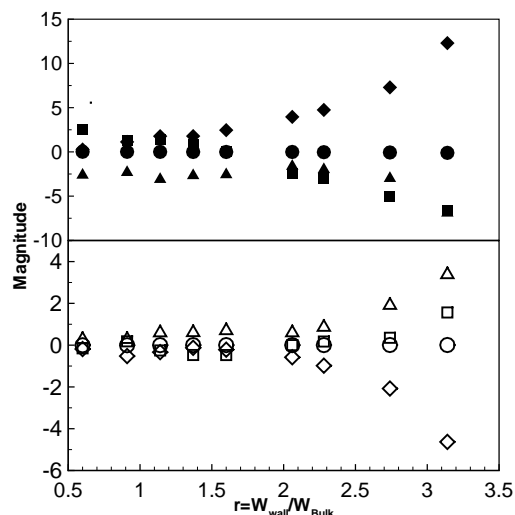


Figure 7. Contribution of mean vorticity against parameter r in the core of vortex. Solid symbols: near the top corner; Open symbols: near the moving wall; \square : Shear term; \triangle : Normal term; \diamond : Diffusion term; \circ : Convection term.

significant, which remain similar to their Poiseuille duct flow counterpart. The major changes reside in the region close to the Couette wall. In the cross sectional view of secondary flow, the two clockwise rotating vortices gradually merge in tandem with speed of the moving wall and form a large clockwise vortex. Also, together with a small counterclockwise corner vortex, this vortex pattern is similar that observed in the corner region of the duct flow with free surface. Beyond $r > 1.6$, slight deviation from the free surface vortex pattern is observed due to the formation of another smaller clockwise rotating vortex near the top corner. This change of vortex structure is also reflected in the dominant terms of the vorticity transport equation. A linear relation is observed to exist between the angle of the vortices and the parameter r . As the ratio of moving velocity continually elevates toward $r > 2.06$, the change of angle saturates.

Different Couette wall strain rates also exert substantial influence on the turbulence structure. With regard to the turbulence kinetic energy, the turbulence intensities are first damped near the moving wall, which is caused by the reduced strain rate $\frac{\partial W}{\partial y}$ in the corresponding region. Due to the reduction of the streamwise velocity fluctuation at the moving wall, turbulence structure gradually moves towards a rod-like axi-symmetric turbulence as r increases. As the wall velocity increases further for $r > 1.2$, the rod like structure disappears, and turbulence reverts to the disk like structure.

REFERENCES

Antonia, R. A., Danh, H. Q. & Prabhu, A. 1977 Response of a turbulent boundary layer to a step change in surface heat flux. *J. Fluid Mech.* **80**, 153–177.
Brogolia, R., Pascarelli, A. & Piomelli, U. 2003 Large eddy simulations of ducts with a free surface. *J. Fluid Mech.* **484**, 223–253.
Gavrilakis, S. 1992 Numerical simulation of low-reynolds-

number turbulent flow through a straight square duct. *J. Fluid Mech.* **244**, 101–129.

Germano, M., Piomelli, U., Moin, P. & Cabot, W. 1991 A dynamic sub grid-scale eddy viscosity model. *Phys. Fluids* **3**, 1760–1765.
Grega, L. M., Wei, T., Leighton, R. I. & Neves, J. C. T. 1995 Turbulent mixed-boundary flow in a corner formed by a solid wall and a free surface. *J. Fluid Mech.* **294**, 17–46.
Hsu, H. W., Hsu, J. B., Lo, W. & Lin, C. A. 2012 Large eddy simulations of turbulent couette-poiseuille and couette flows inside a square duct. *J. Fluid Mech.* **702**, 89–101.
Hsu, H. W., Hwang, F. N., Wei, Z. H., Lai, S. H. & Lin, C. A. 2011 A parallel multilevel preconditioned iterative pressure poisson solver for the large-eddy simulation of turbulent flow inside a duct. *Comput. Fluids* **45**, 138–156.
Huser, A. & Biringen, S. 1993 Direct numerical simulation of turbulent flow in a square duct. *J. Fluid Mech.* **257**, 65–95.
Hwang, C. B. & Lin, C. A. 2003 Low-reynolds-number k-e modeling of nonstationary solid boundary flows. *AIAA J.* **41**, 168–175.
Iacovides, H. & Launder, B. E. 1995 Computational fluid dynamics applied to internal gas-turbine blade cooling: A review. *International J. of Heat and Fluid Flow* **16**, 454–470.
Iwamoto, K., Suzuki, Y. & Kasagi, N. 2002 Reynolds number effect on wall turbulence: toward effective feedback control. *International J. of Heat and Fluid Flow* **23**, 678–689.
Kuroda, A., Kasagi, N. & Hirata, M. 1993 Direct numerical simulation of turbulent plane couette-poiseuille flows: Effect of mean shear rate on the near wall turbulence structures. In *Proc. Turbulent Shear Flows*, p. 241. Springer-Verlag, Berlin.
Lee, M. J. & Reynolds, W. C. 1985 Numerical experiments on the structure of homogeneous turbulence. *Tech. Rep.* Stanford University, Thermoscience Division.
Lilly, D. K. 1992 A proposed modification of the germano subgrid-scale closure method. *Phys. Fluids A* **4**, 633–635.
Lo, W. & Lin, C. A. 2006 Mean and turbulence structures of couette-poiseuille flows at different mean shear rates in a square duct. *Phys. Fluids* **18**, 068103.
Lumley, J. L. 1978 Computational modeling of turbulent flows. *Adv. Appl. Mech.* **18**, 123–176.
Madabhushi, R. K. & Vanka, S. P. 1991 Large eddy simulation of turbulence-driven secondary flow in a square duct. *Phys. Fluids A* **3**, 2734–2745.
Moser, R., Kim, J. & Mansour, N. 1999 Direct numerical simulation of turbulent channel flow up to $Re_{\tau}=590$. *Phys. Fluids* **11**, 943–945.
Pallares, J. & Davidson, L. 2002 Large eddy simulations of turbulent heat transfer in stationary and rotating square ducts. *Phys. Fluids* **14**, 2804–2816.
Thurlow, E. M. & Klewicki, J. C. 2000 Experimental study of turbulent poiseuille-couette flow. *Phys. Fluids* **4**, 865–875.
Uhlmann, M., Pinelli, A., Kawahara, G. & Sekimoto, A. 2007 Marginally turbulent flow in a square duct. *J. Fluid Mech.* **588**, 153–162.
Vazquez, M. Salinas & Metais, O. 2002 Large eddy simulation of the turbulent flow through a heated square duct. *J. Fluid Mech.* **453**, 201–238.